Open access • Journal Article • DOI:10.1103/PHYSREVMATERIALS.5.056001

Engineering nitrogen- and hydrogen-related defects in ZnO nanowires using thermal annealing — Source link

José Villafuerte, Odette Chaix-Pluchery, Joseph Kioseoglou, Fabrice Donatini ...+3 more authors

Institutions: University of Grenoble, Aristotle University of Thessaloniki

Published on: 06 May 2021 - Physical Review Materials (American Physical Society)

Topics: Annealing (metallurgy), Crystallographic defect, Doping, Chemical bath deposition and Hydrogen

Engineering nitrogen- and hydrogen-related defects in ZnO nanowires using thermal annealing

José Villafuerte,[1,2] Odette Chaix-Pluchery,[1] Joseph Kioseoglou,[3] Fabrice Donatini,[2] Eirini Sarigiannidou,[1] Julien Pernot,[2]* and Vincent Consonni[1]*

[1] *Univ. Grenoble Alpes, CNRS, Grenoble INP, LMGP, F-38000 Grenoble, France*

[2] *Univ. Grenoble Alpes, CNRS, Grenoble INP, Institut NEEL, F-38000 Grenoble, France*

[3] *Physics Department, Aristotle University of Thessaloniki, 54124 Thessaloniki, Greece*

* Corresponding Authors: julien.pernot@neel.cnrs.fr and vincent.consonni@grenoble-inp.fr

The chemical bath deposition (CBD) of ZnO nanowires is of high interest, but their formation occurs in a growth medium containing a large number of impurities including carbon, nitrogen, and hydrogen, rendering the accurate determination of predominant crystal defects as highly debated. In addition to the typical interstitial hydrogen in bond-centered sites (H_{BC}) and zinc vacancy – hydrogen (V_{Zn}-nH) complexes, we reveal that the nitrogen-related defects play a significant role on the physical properties of unintentionally-doped ZnO nanowires. In particular, we show by density-functional theory that the (V_{Zn}-N_O-H) defect complex acts as a deep acceptor with a relatively low formation energy and exhibits a prominent Raman line at 3078 cm^{-1} along with a red-orange emission energy of around 1.82 eV in cathodoluminescence spectroscopy. The nature and concentration of the nitrogen- and hydrogen-related defects are found to be tunable using thermal annealing under oxygen atmosphere, but a rather complex, fine evolution including successive formation and dissociation processes is highlighted as a function of annealing temperature. ZnO nanowires annealed at the moderate temperature of 300 °C specifically exhibit one of the smallest free charge carrier density of 5.6 x 10^{17} cm^{-3} along with a high mobility of about 60 cm^2/V s following the analysis of longitudinal optical phonon – plasmon coupling. These findings report a comprehensive diagram showing the complex interplay of each nitrogen- and

hydrogen-related defect during thermal annealing and its dependence on annealing temperature. They further reveal that the engineering of the nitrogen- and hydrogen-related defects as the major source of crystal defects in ZnO nanowires grown by CBD is capital to precisely control their electronic structure properties governing their electrical and optical properties in any devices.

KEYWORDS

ZnO nanowires, chemical bath deposition, hydrogen, nitrogen, defects

I. INTRODUCTION

The optimization and control of the electrical and optical properties of ZnO nanowires (NWs) grown by the widely used low temperature chemical bath deposition (CBD) technique is a critical issue for enhancing the performances of the related piezoelectric [1,2], piezotronic [3], optoelectronic [4], photovoltaic [5], and chemical/biological sensor [6] devices. The accurate knowledge on the nature and concentration of intrinsic/extrinsic point defects governing the electronic structure properties of ZnO NWs is required. In the CBD technique [7], an inherent characteristic originates from the crystallization process of ZnO NWs operating in an aqueous solution, namely in an hydrogen-rich environment [8-10]. Over the last years, the predominant role of hydrogen in unintentionally-doped ZnO NWs grown by CBD has been supported by several chemical, optical, and electrical analyses [11-14]. The presence of hydrogen in the center of ZnO NWs has been detected by nuclear magnetic resonance [11] and elastic recoil detection analysis [12]. The correlated high density of free charge carriers in ZnO NWs has been shown by terahertz spectroscopy [15], scanning probe microscopy [16], field-effect transistor (FET) measurements [17], scanning capacitance microscopy [18], and four-point probe resistivity measurements [13,14]. O- and Zn-polar ZnO nanorods grown by CBD within the selective area growth (SAG) approach were further found to exhibit, on average, a high electrical conductivity of 10.2 and 90.9 S/cm, respectively [13]. Later, ZnO NWs grown by CBD within the spontaneous growth approach were also shown to present, on average, a high electrical conductivity ranging from 35.2 to 243.1 S/cm [14]. These statistical studies have revealed that the high density of free charge carriers in the range of 6.4×10^{17} – 1.1×10^{19} cm^{-3} for selective area grown ZnO nanorods and 2.7×10^{18} – 3.1×10^{19} cm^{-3} for spontaneously grown ZnO NWs is directly attributed to the massive incorporation of hydrogen by using Raman and cathodoluminescence spectroscopy [13,14].

For almost two decades, hydrogen-related defects in ZnO have been addressed by the pioneered work of Van de Walle, revealing, from density-functional theory (DFT) calculations, that interstitial hydrogen (H_i) does not act as an amphoteric impurity as in many other semiconductors, but as a shallow donor over the expected range of Fermi level [19]. Substitutional hydrogen on the oxygen lattice site (H_O) [20], and zinc vacancy – hydrogen (V_{Zn}-nH) defect complexes, where n lying in the range of 1-4 represents

the number of involved H_i atoms [21,22], have further been considered to play a major role. Experimental evidences of the presence of these hydrogen-related defects in ZnO thin films have been pointed out using optical spectroscopy [23-27]. H_i in the bond centered site (H_{BC}) was previously considered as the most stable configuration [19], but a recent study has shown that (V_{Zn}-3H) defect complex presents an even lower formation energy [14]. Hence, H_{BC} and (V_{Zn}-3H) defect complex acting as two shallow donors with a very low formation energy along with H_O have been identified as the major source of n-type conductivity in unintentionally-doped ZnO NWs grown by CBD [13,14].

In the field of piezoelectric devices [1], unintentionally-doped ZnO NWs grown by CBD face the critical challenge of piezoelectric potential screening originating from the high density of free charge carriers in their center [28-31]. Under mechanical stress, a piezoelectric potential is generated along the polar *c*-axis of ZnO NWs from the displacement of the charge centers of anions and cations. For a high concentration of shallow donors, a screening potential created from mobile free electrons is generated in the opposite direction, reducing in turn the overall magnitude of the piezoelectric potential [28]. Through analytical and finite element method simulations, the piezoelectric potential has been found to be strongly reduced as the concentration of shallow donors is increased above 10^{17} cm^{-3} [29-31]. The control of the concentration of shallow donors was thus shown to drastically improve the performance of sound-driven piezoelectric nanogenerators [32]. Additionally, surface Fermi level pinning was theoretically found to compensate for the detrimental effects of the high concentration of shallow donors by depleting the center of ZnO NWs, but only to a limited extent for a high doping level [33]. As a result, the engineering of hydrogen-related defects (*i.e.*, in terms of nature and concentration) in unintentionally-doped ZnO NWs grown by CBD is of high significance. A typical strategy has involved a post-deposition thermal annealing to dissociate hydrogen-related defects and exo-diffuse hydrogen from the bulk of ZnO thin films [34] and NWs [35,36]. Huang et al. showed that a thermal annealing in air can drastically improve the intensity of the near-band edge (NBE) emission in the photoluminescence spectra of ZnO NWs grown by CBD [35]. Urgessa et al. investigated the stability of the I_4 line assigned to H_O in ZnO NWs grown by CBD as a function of annealing temperature [36]. The present approach offers a great opportunity to monitor the nature and concentration of hydrogen-related defects in ZnO NWs, but it has not been explored yet in detail. More recently, the alternative oxygen plasma treatment

in ZnO nanorods has also been found to improve the Schottky contact with Au on their top *c*-plane faces through the strong effects on the nature and concentration of hydrogen-related defects [37]. Furthermore, the growth medium contains hydrogen, but also carbon and nitrogen species. The involvement of hydrogen, carbon, and nitrogen in the same medium is expected to play a significant role as well, for instance by forming additional nitrogen- and hydrogen-based defect complexes [38-41]. However, the nature of these defect complexes and their assignment by using Raman and cathodoluminescence spectroscopy still need to be clarified, specifically in the context of CBD-grown ZnO NWs.

In the present article, the engineering of nitrogen- and hydrogen-related defects is performed by thermal annealing, where a series of isochronal thermal annealed ZnO NWs spontaneously grown by CBD are prepared under oxygen atmosphere in the temperature range of 200 to 1000 °C. The combination of Raman and cathodoluminescence spectroscopy with DFT calculations offers a comprehensive analysis of the evolution of these defects during the annealing process. It also shows the interplay between the nitrogen and hydrogen species in unintentionally-doped ZnO NWs grown by CBD, which should be monitored to tune their electrical and optical properties.

II. EXPERIMENTAL AND THEORETICAL METHODS

A. Synthesis and thermal annealing of ZnO nanowires

(001) silicon substrates were cleaned in an ultrasonic bath using acetone and isopropyl alcohol to remove the residual contaminants. The polycrystalline ZnO seed layers were deposited by dip coating using a sol-gel process. The chemical precursor solution consisted of 375 mM zinc acetate dihydrate ($Zn(CH_3COO)_2.2H_2O$, Sigma-Aldrich) and 375 mM monoethanolamine (MEA, Sigma-Aldrich) mixed in pure ethanol. It was stirred for several hours at 60 °C on a hot plate to obtain a clear solution and then at room temperature to complete the $Zn(CH_3COO)_2$ dilution. The substrates were subsequently dipped into the solution and gently pulled out under a controlled atmosphere (< 15 % hygrometry). They were annealed for 10 min at 300 °C on a hot plate for the evaporation of residual organic compounds and for 1 h at 500 °C in an oven under air for the crystallization of ZnO seed layers. ZnO NWs were grown by CBD in a sealed reactor containing a chemical precursor solution of 30 mM zinc nitrate hexahydrate ($Zn(NO_3)_2.6H_2O$, Sigma-Aldrich) and hexamethylenetetramine (HMTA, Sigma-Aldrich) mixed in

deionized water. The sealed reactor was placed for 5 h in an oven kept at 85 °C. The pH value of around 5.5 was measured during the CBD process. Thermal annealing treatments were eventually performed in a tubular furnace under oxygen atmosphere for 1 h in the temperature range of 200 – 1000 °C.

B. Characterization techniques

The morphology of ZnO NWs was assessed by field-emission scanning electron microscopy (FESEM) imaging using a FEI Quanta 250 FESEM instrument. The nature and concentration of hydrogen-related defects were investigated by Raman and cathodoluminescence spectroscopy. Raman spectroscopy of ZnO NWs was achieved with a Horiba/Jobin Yvon Labram spectrometer equipped with a liquid nitrogen-cooled CCD detector. An Ar^+ laser exhibiting a 514.5 nm line and a power on the sample surface close to 0.64 mW was focused to a spot size close to 1 μm^2 using a 100 times objective. The integration time depended on the spectral region and ranged from 2 min for low wavenumbers corresponding to the ZnO-related typical phonon modes to 1 h for high wavenumbers corresponding to the nitrogen- and hydrogen-related phonon modes. The spectrum calibration was performed at room temperature using a silicon reference sample. The theoretical position of the silicon Raman line was set to 520.7 cm^{-1}. 5 K cathodoluminescence measurements were performed on single ZnO NWs dispersed on SiO_2/Si substrates with a FEI Inspect F50 FESEM instrument equipped with a liquid helium-cooled stage. The cathodoluminescence signal was collected through a parabolic mirror and analyzed with a 550 mm focal length monochromator equipped with 600 grooves/mm diffraction grating. Cathodoluminescence spectra were recorded with a thermoelectric cooled silicon CCD detector. A low acceleration voltage of 5 kV and a small spot size (*i.e.*, less than 10 nm) were used to focus the acquisition on the single ZnO NW.

C. Density-Functional Theory Method

The study about the wurtzite structure of ZnO and of the related point defects was carried out using the VASP code with projector augmented-wave (PAW) potentials [42,43] under the Perdew-Burke-Ernzerh derivation of the generalized gradient approximation (GGA-PBE) [44,45] of the DFT. A Monkhorst-Pack mesh of 8x8x6 for the 1x1x1 unit cell was set to define the reciprocal-space resolution corresponding to the *k*-point mesh generation. The *k*-point mesh was *Γ*-centred and the cut-off energy

was set to 600 eV. A 4x4x3 supercell composed of 192 atoms was used to ensure the structural relaxation and the accurate calculations of the optoelectronic properties of point defects in ZnO. Extensive tests concluded that these properties cannot be accurately determined in smaller size supercells. The convergence with respect to *k*-point sampling, slab and vacuum thickness was explicitly checked. The DFT+*U* method was selected to accurately calculate the electronic structure and optical properties, as a computational cost-efficient method in large size supercells [46]. The values of the Hubbard parameters *U* were incorporated for the *d*-states of Zn ($U_{d,Zn}$) and *p*-states of O ($U_{p,O}$) to produce good lattice constants and band gap energy of 3.4 eV for ZnO [47]. The following *U* values were taken [48]: $U_{d,Zn}$=10.5 eV and $U_{p,O}$=7.0 eV. The application of self-consistent values of *U* produces electronic structures that are in better agreement with hybrid functional calculations, as well as almost universally in better agreement with the experimental lattice geometry [49]. The *s*-states of H were treated at the PBE level, which is a common approach for these atoms. The *p*-states of N were introduced using the same *U* value as the *p*-states of O: $U_{p,N}$=7.0 eV. The present assumption considering $U_{p,N}$= $U_{p,O}$ as reported in Refs. [46,50,51] is realistic and consistent due to the fact that N atoms substitute for O atoms in the ZnO lattice, The oxygen chemical potential μ_O was set to -2.11 eV, corresponding to intermediate growth conditions. The formation energies of each complex point defect were computed using the well-established formalisms described in Ref. [52], whose the main expression was given in Ref. [14]. The luminescence positions of the (V_{Zn}-N_O-H) defect complex were calculated for the different transition levels within the Franck-Condon approximation using the effective one-dimensional configuration coordinate to get the zero phonon line energy (E_{ZPL}), emission energy ($E_{emission}$), and absorption energy ($E_{absorption}$), as presented in Refs. [14,53,54].

III. RESULTS AND DISCUSSION

A. Morphological properties of as-grown and annealed ZnO nanowires

The CBD of unintentionally-doped ZnO NWs on a *c*-axis oriented polycrystalline ZnO seed layer deposited by dip coating on silicon was performed at 85 °C and at a pH value of around 5.5 using $Zn(NO_3)_2$ and HMTA [55,56]. The as-grown ZnO NWs were annealed for 1 h in a tubular furnace under oxygen atmosphere in the temperature range of 200 to 1000 °C. The morphology of as-grown and

annealed ZnO NWs is presented in **Fig. 1** by FESEM imaging. Prior to the thermal annealing, as-grown ZnO NWs are vertically aligned with a hexagonal shape that is typical of their wurtzite structure along the polar *c*-axis [57]. They exhibit a mean diameter and length of 100 ± 27 and 1560 ± 71 nm, respectively [14]. In the annealing temperature range of 200 – 800 °C, no change of the morphology of ZnO NWs is shown, indicating their morphological stability as expected from the high melting point of ZnO around 2248 K [58]. As the annealing temperature is raised to 900 °C, ZnO NWs start to coalesce to a larger extent and their hexagonal shape is less pronounced. At an annealing temperature of 1000 °C, ZnO NWs have a wavy structure and their hexagonal shape is completely lost at the benefit of a cylinder shape. From 900 °C, ZnO thin films and NWs typically undergo recrystallization phenomena through diffusive transport process, leading to a structural reordering that was previously used to transform ZnO thin films into NW arrays [59].

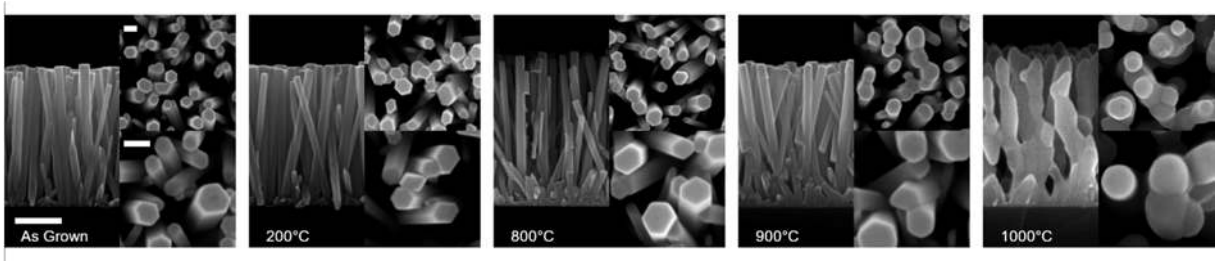

FIG. 1. Cross-sectional- and top-view FESEM images of unintentionally-doped ZnO NWs grown by CBD and annealed for 1 h under oxygen atmosphere in the temperature range of 200 to 1000 °C. The scale bars correspond to 500 and 100 nm for the cross-sectional- and top-views, respectively.

B. Raman spectroscopy of as-grown and annealed ZnO nanowires

The Raman scattering spectra of as-grown and annealed ZnO NWs are presented in **Fig. 2** with a zoom-in in the area of interest in **Fig. S1**. In the low wavenumber range of 50 – 900 cm^{-1}, the optical phonon modes observed in as-grown NWs are located at 99 (E_2^{low}), 378 (A_1(TO)), 438 (E_2^{high}), and 574 (A_1(LO)) cm^{-1}, showing the wurtzite structure of ZnO NWs [60]. Second-order Raman lines occur at 203 (2TA/$2E_2^{low}$), 483 (2LA), 666 (TA+LO), and 812 (LA+TO) cm^{-1}. The Raman line at 333 cm^{-1} corresponds to the E_2^{high}-E_2^{low} mode,[18] but the involvement of the 1s → 2p donor state transition assigned to H_{BC} may also take place [25]. No additional modes related to residual extrinsic impurities including aluminium, gallium, iron, and antimony are detected [61]. The low value of pH around 5.5 along with

the absence of chemical additives including these dopants exclude the significant incorporation of residual extrinsic impurities [62,63] other than hydrogen, carbon, and nitrogen present in the chemical precursors and growth medium. Nevertheless, no additional mode related to nitrogen substituting for the oxygen lattice site (N_O) is detected either [64]. As the annealing temperature is raised from 200 to 1000 °C, the nature of the optical phonon modes does not differ. However, the significant increase in the intensity of the E_2^{high} mode along with the decrease in its full-width-at-half maximum (FWHM) from 17.5 to 10.1 cm^{-1} as seen in **Fig. S2** highlight an improvement of the crystallinity of annealed ZnO NWs through restoring and recrystallization phenomena. Correlatively, the line position of the E_2^{high} mode shifts towards lower wavenumbers until its stabilization at around 437.6 cm^{-1}, indicating a possible relaxation of the wurtzite structure of ZnO NWs.

In the high wavenumber range of 2750 – 3750 cm^{-1}, a large number of Raman lines are associated with the presence of hydrogen, carbon, and nitrogen. From 2750-3000 cm^{-1}, several sharp Raman lines at 2890, 2918, 2948, and 2988 cm^{-1} are attributed to the antisymmetric and symmetric stretching bonds of $C–H_X$ groups (x = 1, 2, 3) [38], originating from the residual HMTA molecules adsorbed on the nonpolar *m*-plane sidewalls of ZnO NWs [56,65,66]. Carbon-related species are thus detected only on the surfaces of ZnO NWs. A prominent Raman line at 3078 cm^{-1} with a FWHM of 24.1 cm^{-1} along with two weak lines at 3121 and 3160 cm^{-1} also occur as shown in **Fig. 3** and typically lies in the wavenumber range where the phonon modes are associated with nitrogen-related bonds [38-41,67]. Nickel et al. identified a Raman line at 3096 cm^{-1} tentatively assigned to the stretching vibration of the $N_O–H$ bonds [38]. Li et al. showed the presence of a line at a wavenumber of 3020 cm^{-1} using infrared absorption spectroscopy [39]. From DFT calculation, they revealed that N_O^- and H_i^+ have a high probability of forming neutral $N_O–H$ defect complex in the antibonding configuration both in perpendicular ($AB_{N\perp}$) and parallel ($AB_{N\parallel}$) positions, exhibiting the lowest formation energies. Depending on the pseudopotentials used, two respective infrared modes with a corresponding line at 3055/3117 cm^{-1} and 3084 cm^{-1} were calculated. Also, the breaking of the $N_O–H$ bonds requires an energy larger than 1.25 eV, highlighting its high stability [67]. Correlatively, Jokela et al. unambiguously identified a $N_O–H$ bond-related phonon mode giving rise to a line at 3150.6 cm^{-1} using infrared absorption spectroscopy [40,41]. Kumar et al. correspondingly showed the presence of the same line around 3150 cm^{-1} using

Raman spectroscopy [68]. From these theoretical and experimental investigations, the Raman lines at 3121 and 3160 cm^{-1} separated by around 40 cm^{-1} are attributed to the N_O–H bonds in the $AB_{N\perp}$ and $AB_{N//}$ configurations, respectively. These N_O–H bonds are located on the surfaces of ZnO NWs when originating from the residual HMTA molecules [56], and in their center *via* the related (N_O-H) defect complex. More importantly, a Raman line at 3078 cm^{-1} was assigned to the (V_{Zn}-N_O-H) defect complex as a presumably single shallow acceptor with an ionization energy of 134 meV [69], stabilizing the (V_{Zn}-N_O) defect complex [70]. The line position of (V_{Zn}-N_O-H) defect complex perfectly fits our line in the present Raman spectra. The nature of this defect complex is however highly debated as recent DFT calculations have reported its deep [71] or shallow [72] acceptor character. As a consequence, it turns out that our prominent Raman line pointing at 3078 cm^{-1} is attributed to the (V_{Zn}–N_O–H) defect complex presumably located on the surfaces of ZnO NWs and in their center. During the CBD process, the solubilization of $Zn(NO_3)_2$ in aqueous solution results in the formation of Zn^{2+} and NO_3^- ions, which may be favorable for the incorporation of a significant amount of nitrogen in the center of ZnO NWs. From 3200 - 3750 cm^{-1}, several additional Raman lines related to hydrogen in different forms and located on the surfaces and in the center of ZnO NWs take place. An asymmetric broad Raman band centered at 3575 cm^{-1} involves a dominant Raman line assigned to H_{BC} [24,73], and a shoulder around 3500 cm^{-1} attributed to O–H bonds [24,69,74] on the surfaces of ZnO NWs. Another asymmetric broad Raman band centered around 3375 cm^{-1} involves the contribution of (V_{Zn}-*n*H) defect complexes in the wavenumber range of 3300 – 3418 cm^{-1}, mainly (V_{Zn}-H) [24,53], (V_{Zn}-2H) [24], and (V_{Zn}-3H) [75] defect complexes.

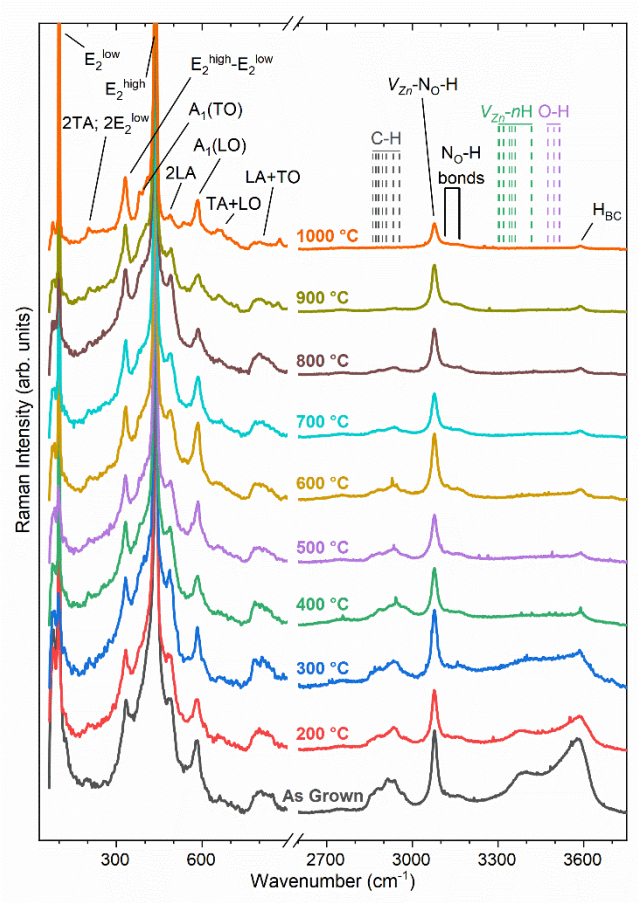

FIG. 2. Raman spectra of unintentionally-doped ZnO NWs grown by CBD and annealed for 1 h under oxygen atmosphere in the temperature range of 200 to 1000 °C. The insets delimit the calculated and experimental vibrational frequencies from Raman and infrared absorption spectroscopy as deduced from Refs. [14,24,53,69,74,75].

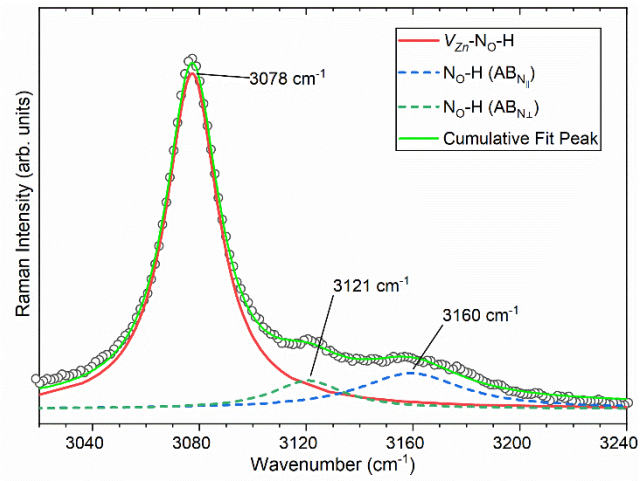

FIG. 3. Zoom-in in the area of interest corresponding to the Raman lines assigned to the nitrogen-related defects in ZnO NWs grown by CBD and annealed for 1 h under oxygen atmosphere at 600 °C. The three

Raman lines assigned to nitrogen-related defects are fitted by Lorentzian functions to decouple their contribution to the experimental data.

Following the assignment of all the Raman lines attributed to nitrogen- and hydrogen-related defects, the Raman spectra were normalized with respect to the line assigned to the E_2^{high} mode and the relative intensity of each line was determined by fitting its area by a Lorentzian function. The evolution of the relative intensity of the Raman lines attributed to nitrogen- and hydrogen-related defects with the annealing temperature is presented in logarithmic scale in **Fig. 4**. At the annealing temperature of 200 °C, a strong decrease in the relative intensity of around 50 % is shown for both Raman lines assigned to H_{BC} and (V_{Zn}-nH) defect complexes, with a significant steady decrease in the annealing temperature range of 400 – 1000 °C. At the annealing temperatures of 300 and 600 °C, an increase in the relative intensity of both Raman lines assigned to H_{BC} and (V_{Zn}-nH) defect complexes is revealed. This increase is more pronounced for the Raman line ascribed to (V_{Zn}-nH) defect complexes in ZnO NWs annealed at 300 °C and for the Raman line attributed to H_{BC} in ZnO NWs annealed at 600 °C. This specific behavior was previously reported partly by Koch et al., showing that H_{BC} forms electrically inactive interstitial hydrogen molecules (H_2) after a thermal annealing at low temperature [34]. The further increase in the annealing temperature makes H_{BC} energetically favorable as compared to H_2 molecules, resulting in its dissociation and in the reappearance of H_{BC} with a maximum concentration in the range of 650 – 700 °C [34]. In our case, the formation of interstitial H_2 molecules at the expense of H_{BC} accounts for the sharp decrease in the relative intensity of this mode at the annealing temperature of 200 °C. However, the further increase in the annealing temperature could make energetically favorable the formation of not only H_{BC}, but also other hydrogen-related defects such as C-H_X, (V_{Zn}-nH), (N_O-H), and (V_{Zn}-N_O-H) defect complexes, hence explaining the sharp increase of the Raman lines related to these defects at the annealing temperatures of 300 and 600 °C. The Raman lines assigned to N_O–H bonds and (V_{Zn}-N_O-H) defect complex present a greater stability since only a 30 % decrease in their relative intensity is shown in ZnO NWs annealed at 200 °C together with a small variation up to the annealing temperatures of 800 - 900 °C [69]. In particular, the evolution of the relative intensities of the N_O–H bonds in $AB_{N//}$ configuration and of (V_{Zn}-N_O-H) defect complex is very similar, whereas the evolution of the relative

intensity of the N_O–H bonds in $AB_{N\perp}$ configuration significantly differs in the annealing temperature range of 700 – 900 °C. Gao et. al. stated that the thermal annealing of nitrogen-doped ZnO NWs under oxygen atmosphere at temperatures above 500 °C promotes the exo-diffusion of N_O *via* an oxygen vacancy-assisted mechanism [76], as supported by DFT calculations [77]. However, this diffusion mechanism is expected to occur gradually, since N_O is systematically compensated by H_i, and residual amounts of N_O-H and (V_{Zn}-N_O-H) defect complex have been shown up to an annealing temperature of 800 °C [69,76], which is even higher here and around 1000 °C. Hence, an interplay between the contributions from both defects with a different thermal stability is expected to account for the evolution of the present Raman lines. It should also be noted that, at the annealing temperature of 1000 °C, the Raman lines attributed to N_O–H bonds and (V_{Zn}-N_O-H) defect complex and, followed by H_{BC}, present the most prominent intensities for the nitrogen- and hydrogen-related defects. The relative thermal stability of the C–H_X bonds also confirms that they are trapped on the *m*-plane sidewalls of ZnO NWs, hence requiring high annealing temperatures for activating efficient desorption phenomena starting at the annealing temperature of 700 °C.

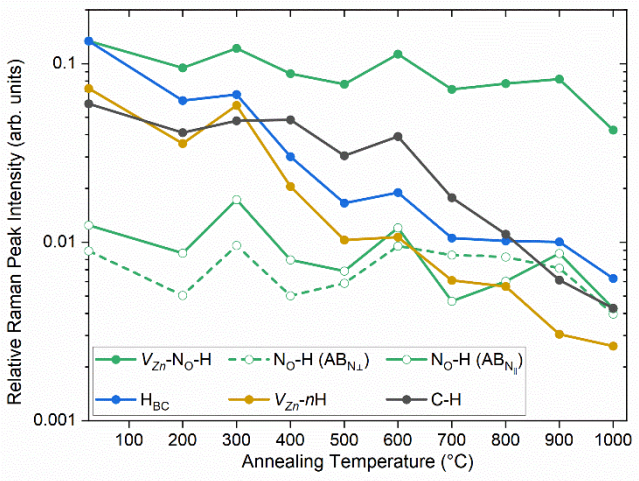

FIG. 4. Evolution of the relative intensity of the Raman spectrum lines assigned to hydrogen-related defects of unintentionally-doped ZnO NWs grown by CBD and annealed for 1 h under oxygen atmosphere in the temperature range of 200 to 1000 °C. The first data point is related to as-grown ZnO NWs.

C. Structure of crystal defects using density functional theory

The role of the (V_{Zn}-N_O-H) defect complex in ZnO was carefully investigated by DFT calculations in the same conditions as in Ref. [14], using the VASP code with PAW potentials [42,43] under the GGA-PBE [44,45]. The formation energy of the (V_{Zn}-N_O-H) defect complex as a function of the Fermi level is presented in **Fig. 5a** along with the formation energies of V_{Zn} and (V_{Zn}-H) defect complex for direct comparison. The transition levels of the different thermodynamic charge states of V_{Zn}, (V_{Zn}-H), and (V_{Zn}-N_O-H) defect complexes are gathered in **Fig. 5b**.

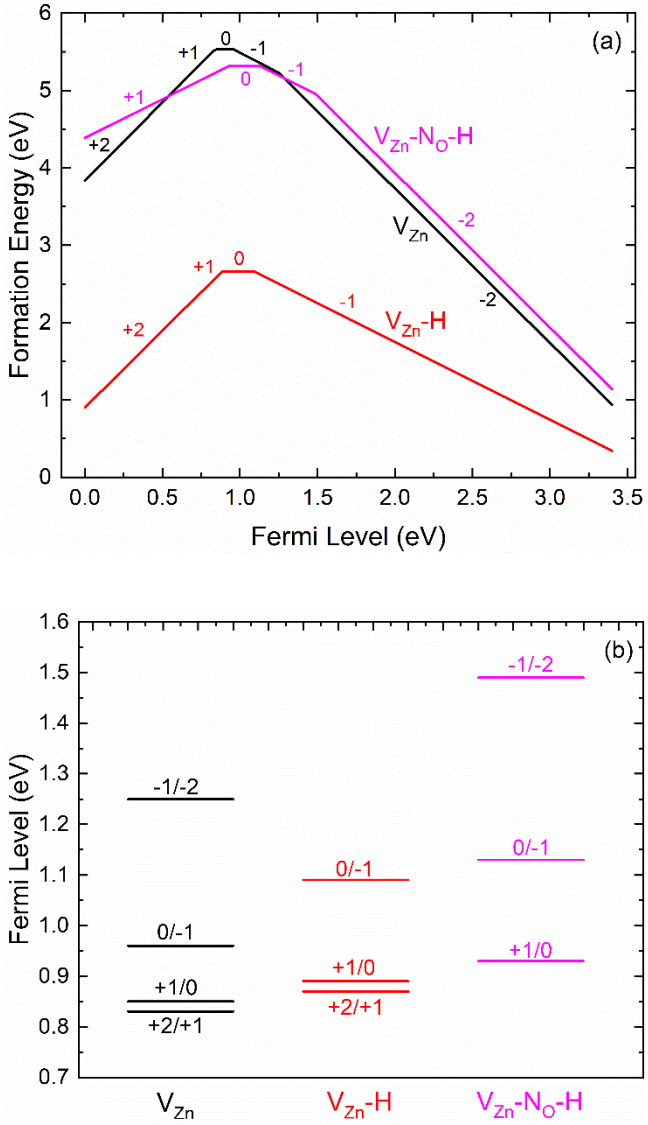

FIG. 5. (a) Formation energies of nitrogen- and hydrogen-related defects in ZnO as a function of the Fermi level determined by DFT calculations. The most stable configuration with the lowest energy is presented for each charge state. The zero of Fermi energy was set at the VBM. Chemical potential values

of μ_O = -2.11 eV and μ_H = -0.475 eV were employed. (b) Transition levels of each of V_{Zn}, (V_{Zn}-H), and (V_{Zn}-N_O-H) defects as a function of the vertically aligned Fermi level.

As reported in a number of investigations using DFT calculations [14,53,54] and in **Fig. 5a,** V_{Zn} and (V_{Zn}-H) defect complex act as deep acceptors with a -2 and -1 charge state, respectively, when the Fermi level is close to the CBM. The formation energy of the (V_{Zn}-H) defect complex is smaller than the formation energy of V_{Zn} for intermediate conditions, showing its efficient passivation by one H_i atom. The addition of one or two H_i atoms to the (V_{Zn}-H) defect complex results in the formation of stable (V_{Zn}-2H) and (V_{Zn}-3H) defect complexes, the latter being a shallow donor with the +1 charge state and exhibiting the lowest formation energy regardless of the Fermi level in the bandgap [14]. The addition of N_O in ZnO has been investigated in detail using DFT calculations [39,67,71,72]. N_O typically acts as a deep acceptor with a -1 charge state and a relatively large formation energy when the Fermi level is close to the CBM for intermediate and O-rich conditions [39]. In the ZnO NWs grown by CBD where the hydrogen concentration is large [14] and given that hydrogen has a low migration barrier in ZnO [78], the following reaction spontaneously occurs because the formation energy of N_O-H defect is lower than the sum of the formation energies of the individual N_O and H species [39,67,72]:

$$N_O + H \rightarrow N_O\text{-}H \qquad (1)$$

The formation of N_O is thus unlikely in ZnO NWs grown by CBD at the benefit of the (N_O-H) defect complex as revealed in the Raman spectra of **Fig. 2**, showing no additional modes related to N_O in the low wavenumber range [64], but instead the occurrence of two lines associated with N_O–H bonds at 3121 and 3160 cm^{-1} [38]. It should further be noted that the formation of N_{Zn} is even less likely in the present conditions [70]. Additionally, in the ZnO NWs grown by CBD where the concentration of V_{Zn} is large [14], the following reaction spontaneously proceeds as well to form the (V_{Zn}-N_O-H) defect complex [72]:

$$N_O\text{-}H + V_{Zn} \rightarrow V_{Zn}\text{-}N_O\text{-}H \qquad (2)$$

In contrast, the formation of (V_{Zn}-N_O) defect complex is unlikely when the hydrogen concentration is large. The formation energy of the (V_{Zn}-N_O-H) defect complex lies in the same range as the formation energy of V_{Zn} and appears slightly larger than the one of the (V_{Zn}-H) defect complex when the Fermi

level is close to the CBM for intermediate conditions, as shown in **Fig. 5a**. The (V_{Zn}-N_O-H) defect complex acts as a deep acceptor with a -2 charge state, which is in agreement with the hybrid functionals study reported in Ref. [71]. The density-of-states (DOS) of the (V_{Zn}-N_O-H) defect complex using the PyProcar Python package [79] is presented in **Fig. S3**. The O(p) and N(p) states in the band gap are found to coincide, which is in accordance with the corresponding hybrid functionals study [53]. The (-1/-2) transition level lies at 1.49 eV above the VBM, as represented in **Fig. 5b**. The stable atomic configurations of the (V_{Zn}-N_O-H) defect complex in the relaxed wurtzite structure are presented in **Fig. 6**. In order to investigate the structural configurations of the (V_{Zn}-N_O-H) complex defect, all the possible atomistic configurations have been considered taking into account the neutral, +1, -1 and -2 charge states. Initially, the N atom has been considered to substitute an O undercoordinated atom in one of the three basal neighboring positions of the V_{Zn} as well as the axial O undercoordinated atom. Moreover, the H atom has been examined to be bonded with the N atom as well as with the rest of O undercoordinated atoms. In all the cases, the energetically favorable H bond interaction is found to be the H-N by about 0.4 -0.5 eV with respect to the H-O. On the other hand, the substitution of the axial O undercoordinated atom by an N atom is found to be energetically favorable with respect to the basal substitution by only 0.04 eV, for all the examined charge states.

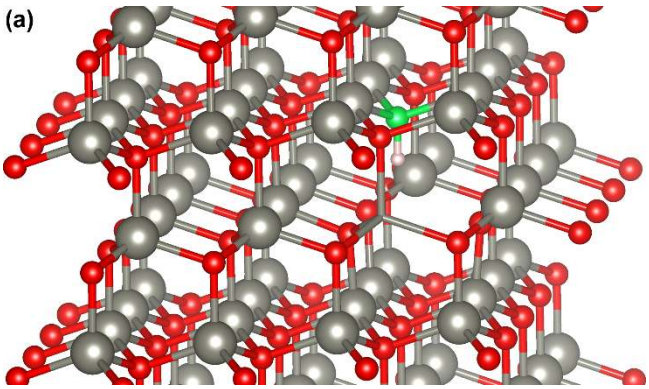

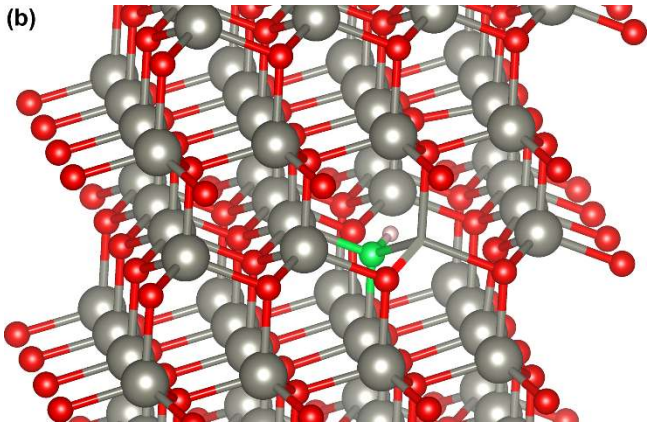

FIG. 6. Structural models for the most stable atomic configuration of the (V_{Zn}-N_O-H) defect complex. In (a), the axial (V_{Zn}-N_O-H) defect complex is represented. In (b), the basal (V_{Zn}-N_O-H) defect complex is represented. The axial configuration is found to be energetically favorable by 0.04 eV with respect to the basal one. Large grey balls, small red balls, small green balls, and small pink balls denote zinc, oxygen, nitrogen, and hydrogen atoms, respectively. The zinc atom in front of the V_{Zn} was taken out for the sake of clarity and only its bonds with the neighboring oxygen atoms are represented.

The luminescence positions of the (V_{Zn}-N_O-H) defect complex for the different transition levels are reported in **Table 1**. In the expected thermodynamic charge state, the (V_{Zn}-N_O-H) defect complex notably exhibits an emission energy of 1.82 eV corresponding to the (-1/-2) transition level.

	Transition level	$E_{transition}$ (eV)	$E_{emission}$ (eV)	E_{ZPL} (eV)	$E_{absorption}$ (eV)
V_{Zn}-N_O-H	ε(+1/0)	0.93	2.50	2.47	2.67
	ε(0/-1)	1.13	2.27	2.27	2.63
	ε(-1/-2)	1.49	1.82	1.91	2.28

TABLE 1. Effective parameters for the computed luminescence transitions of the (V_{Zn}-N_O-H) defect complex.

D. Cathodoluminescence spectroscopy of as-grown and annealed ZnO nanowires

The 5 K cathodoluminescence spectra of as-grown and annealed single ZnO NWs are presented in **Fig. 7a**. The near-band edge (NBE) emission of as-grown ZnO NWs is marked by the dominant contribution of radiative transitions involving neutral donor-bound A-excitons (D^0X_A) around 3.369 eV

with a FWHM of 39.5 meV, as revealed in **Fig. 7b** and **S4**. The involvement of the I_4 and I_5 lines at 3.3628 and 3.3614 eV assigned to H_O and (V_{Zn}-3H) defect complex, respectively, proceeds in that energy range [14,25-27]. Additionally, H_{BC} involved in a line around 3.360 eV also contributes to the NBE emissions [14,25]. As the annealing temperature is increased up to 300 °C**,** a significant 6.7 meV red-shift of the NBE emissions of annealed ZnO NWs is induced, as seen in **Fig. S4**. At the annealing temperature of 500 °C, the NBE emission centered at 3.363 eV lies in the energy range of radiative transitions involving ($D°X_A$). However, its FWHM broadens to the highest value of 50.9 meV, suggesting an important contribution of radiative transitions involving neutral acceptor-bound A excitons ($A°X_A$) [80]. At the annealing temperature of 600 °C, a prominent red-shift of 15.2 meV centers the NBE emissions of annealed ZnO NWs at 3.354 eV, where radiative transitions involving ($A°X_A$) are mostly involved [80]. The increase in the contribution of ($A°X_A$) emissions very well correlates the highest (V_{Zn}-N_O-H) to H_{BC} relative intensity ratio from the corresponding Raman lines, as depicted in **Fig. S5**. This might again indicate that the (V_{Zn}-N_O) defect complex [70] is more favorable for trapping the dissociated H_i atom [69] than a single V_{Zn}. Starting from 700 °C, the high crystalline quality of annealed ZnO NWs is inferred by the overall appearance of longitudinal optical- (LO) phonon replicas separated each other by a phonon energy of around 72 meV in ZnO [26]. The 3.289, 3.219, 3.149 eV lines are associated with the first, second, and third LO phonon replicas of ($D°X_A$) transitions. The presence of the second-order of the NBE emissions (2° NBE) also occurs at about 1.68 eV [81]. The spectra recorded on ZnO NWs annealed at 800 and 900 °C, to a smaller extent, contain a prominent shoulder around 3.31 eV, which has usually been related to ($A°X_A$) [82,83], donor-acceptor pair (DAP) [84-86], and free electron-to-acceptor (FA) [87] transitions in nitrogen-doped ZnO films and NWs. The line at 3.248 eV further represents the first LO phonon replica of the FA transitions (FA-1LO). The nature of the nitrogen-related defects involved in this line is however still under debate. The contribution of N_O can be excluded here as no related additional modes in the Raman spectra in **Fig. 2** occur. More recently, Reynolds et al. correlated the presence of this line related to FA transitions with the formation of the (V_{Zn}-N_O-H) defect complex [69]. However, this line does not occur in ZnO NWs annealed at a lower temperature, while the Raman line at 3078 cm^{-1} clearly takes place in **Fig. 2**, which somehow contradicts the present assignment to the (V_{Zn}-N_O-H) defect complex. At the annealing temperatures of

900 and 1000 °C, the NBE emissions are considerably narrower and dominated by radiative transitions involving ($D^{\circ}X_A$), where a drastic decrease in the FWHM from 39.5 down to 4.7 meV is shown in **Fig. S4**. At the annealing temperature of 1000 °C, the FA transitions have been vanished, suggesting the disappearance of the associated defects. At this high annealing temperature, the narrow line from the NBE emission is centered on the I_4 line and presents a shoulder located around 3.33 eV, originating from the corresponding two-electron satellite (TES) transitions [26]. As a result, both transitions show the predominance of residual H_O in ZnO NWs annealed at 1000 °C. Additionally, the presence of residual H_{BC} as revealed in **Fig. 2-4** also contributes to the NBE emissions at this annealing temperature.

The emissions in the visible spectral region correspond to the dominant broad red-orange band centered at 1.86 eV and to the yellow-green band centered at 2.22 eV, which have been attributed to the (0/-1) and (+1/0) transition levels of the (V_{Zn}-H) and (V_{Zn}-2H) defect complexes formed in the bulk of ZnO NWs, respectively [14]. Interestingly, the red-orange emission band also involves the contribution of the (-1/-2) transition level of the (V_{Zn}-N_O-H) defect complex with an emission energy of 1.82 eV, as reported in **Table 1**. The red-orange emission band is thus related to two different deep acceptors (*i.e.*, (V_{Zn}-H) and (V_{Zn}-N_O-H)), but the decoupling of each contribution is not straightforward due to the proximity of both emission energies. The yellow-green emission band is instead related to the neutral (V_{Zn}-2H) defect complex with no electrical activity [14]. An additional contribution from the (0/-1) transition level of the (V_{Zn}-N_O-H) defect complex located on the surfaces of ZnO NWs may proceed at 2.27 eV. The green-blue emission band centered at 2.68 eV is attributed to V_{Zn} as well as nitrogen- and hydrogen-related defects located on the surfaces of ZnO NWs, including (V_{Zn}-H),[14] (V_{Zn}-2H) [14], and (V_{Zn}-N_O-H) defect complexes with the emission energies of around 2.50 eV corresponding to the (+1/0) transition level. These unexpected charge states in the transition levels of hydrogen-related defects are due to the generation of electron / hole pairs under electron beam and to the further migration of holes towards the surfaces of ZnO NWs where they are highly concentrated owing to upward band-bending [14], which is related to the surface depletion region originating from the adsorbed oxygen ions [88].

Following the assignment of the radiative transitions to nitrogen- and hydrogen-related defects in the visible region of the electromagnetic spectrum, the relative intensity of each emission band was

determined by fitting its area by a Lorentzian function, as depicted in **Fig. S6**. The evolution of the intensity of each visible emission band with annealing temperature is presented in logarithmic scale in **Fig. 8**. Both the red-orange and yellow-green emission bands exhibit a steady decrease in their relative intensity from the annealing temperatures of 200 to 400 °C, reaching a ~64 % decrease at 400 °C. In contrast, the relative intensity of the green-blue emission band stabilizes at the annealing temperature of 200 °C after a significant drop and reaches a ~54 % decrease at the annealing temperature of 400 °C. This steady decrease in the relative intensity of the visible emission bands in **Fig. 8** is in very good agreement with the variation of the relative intensity of the Raman lines assigned to hydrogen-related defects in **Fig. 4**. At the annealing temperature of 500 °C, a general increase in the relative intensity of the visible emission bands correlates with the previously discussed broadening of the NBE emission, which appears to be due to the activation and generation processes of (V_{Zn}-N_O-H) defect complex. The thermal annealing at this temperature under oxygen atmosphere promotes the formation of N_O–H bonds [76], and could be accompanied with the formation of (V_{Zn}-*n*H) defect complex with a low coordination in the center and on the surfaces of ZnO NWs [37]. This can lead to the formation of (V_{Zn}-N_O-H) defect complex on the surfaces of ZnO NWs where holes are highly concentrated under electron beam excitation [14], leading to transition levels other than the expected (-1/-2) one. This statement is very well supported by the largest increase in the relative intensity of the yellow-green emission band, which is related to the (+1/0) and (0/-1) transition levels of the (V_{Zn}-2H) and (V_{Zn}-N_O-H) defect complexes. The formation of the (V_{Zn}-N_O-H) defect complex following a thermal annealing at 450 °C has also been reported by Reynolds et al. [69]. Further thermal annealing from 600 to 900 °C shows that the red-orange and green-blue emission bands have a steady decrease in the relative intensity. In contrast, the yellow-green emission band presents a small increase at the annealing temperatures of 700 and 900 °C, which is somehow in agreement with the evolution of the relative intensity of the Raman lines assigned to N_O–H bonds and (V_{Zn}-N_O-H) defect complex in **Fig. 4**. The red-orange and green-blue emission bands show a strong annihilation at the annealing temperature of 1000 °C, hence revealing the complete disappearance of (V_{Zn}-*n*H) defect complexes both in the bulk and on the surfaces of ZnO NWs, which is in accordance with the Raman spectra in **Fig. 2**. The yellow-green emission band also reveals a significant decrease in its relative intensity, but not a complete annihilation suggesting that the residual

(V_{Zn}-N_O-H) defect complex still occurs as further indicated by the less intense Raman line at 3078 cm^{-1} recorded after thermal annealing at 1000 °C.

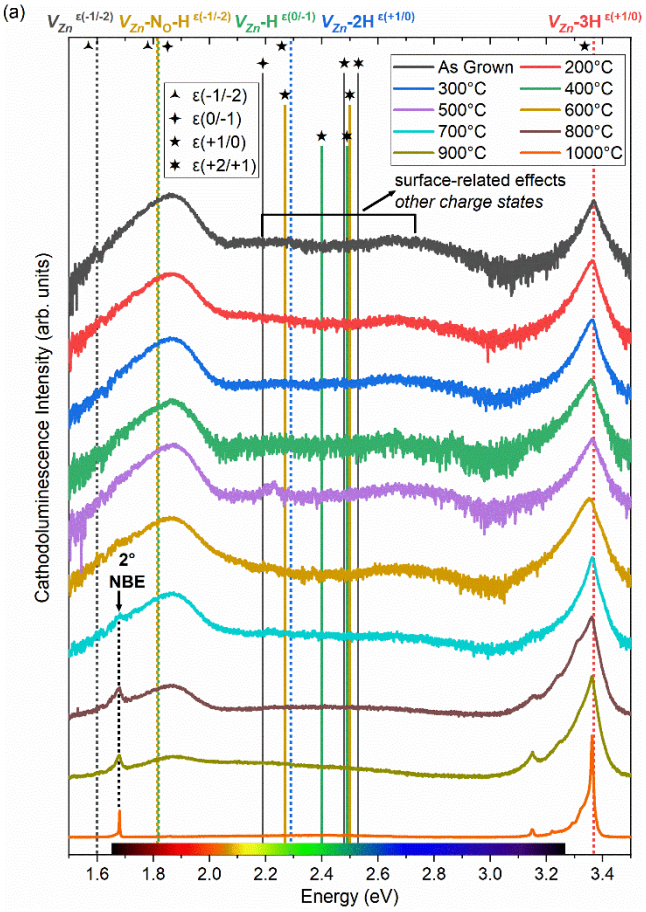

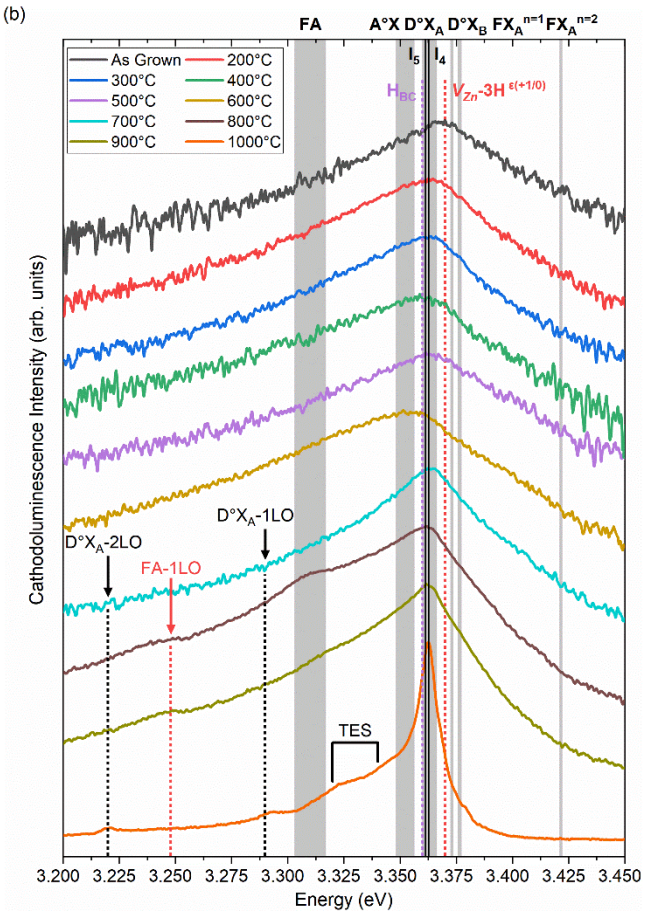

FIG. 7. (a) 5 K cathodoluminescence spectra of unintentionally-doped single ZnO NWs grown by CBD and annealed for 1 h under oxygen atmosphere in the temperature range of 200 to 1000 °C. The insets represent the emission energy of transitions as inferred from DFT calculations in this work and in Refs. [14,53,54]. (b) Corresponding NBE emission regions. The inset represent the emission energy of transitions as deduced from DFT calculations in this work and from experimental data in Refs. [14,25,27].

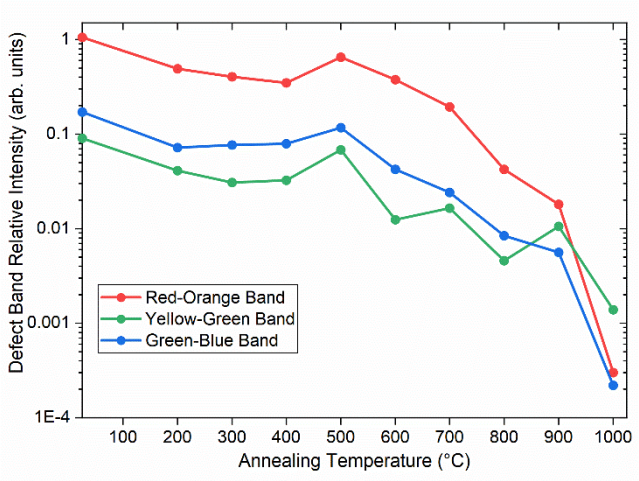

FIG. 8. Evolution of the relative intensity of 5 K cathodoluminescence spectrum bands in the visible part of the electromagnetic spectrum of unintentionally-doped ZnO NWs grown by CBD and annealed for 1 h under oxygen atmosphere in the temperature range of 200 to 1000 °C. The first data point is related to as-grown ZnO NWs.

E. Investigation of the longitudinal optical phonon-plasmon coupled modes

Following the determination of the optical properties of as-grown and annealed ZnO NWs, their free charge carrier density and mobility were extracted by using Raman spectroscopy through the investigation of the coupling between the LO phonons and plasmons. When the LO phonon frequency is close to the free charge carrier plasmon frequency, their macroscopic electric fields strongly interact and couple, hence leading to the creation of LO phonon-plasmon (LPP) coupled modes. This methodology has been widely used in polar semiconductors and early reported for SiC and GaN bulk materials [89-91] and lately for Si-doped GaN wires grown by metal-organic vapor phase epitaxy [92], and ZnO rods grown by chemical vapor deposition [93].

In as-grown and annealed ZnO NWs, their free charge carrier density (n) and mobility (μ) were evaluated *via* a line-shape fitting, in which both the contributions of the electro-optical mechanisms and of the deformation potential were taken into account [89]. The Raman scattering efficiency is then defined by the following equations:

$$I(\omega) \propto [1, C, C^2] \times Im\left[\frac{1}{\varepsilon(\omega)}\right] \text{ and}$$

$$\varepsilon(\omega) = \varepsilon_\infty \times \left[1 + \frac{\omega_{LO}^2 - \omega_{TO}^2}{\omega_{TO}^2 - \omega^2 - i\gamma\omega} - \frac{\omega_P^2}{\omega^2 + i\gamma_P\omega}\right]$$

where $\varepsilon(\omega)$ is the dielectric function, ω is the Raman shift, ε_∞=3.68 is the high frequency dielectric constant of ZnO [94]. C = 6.4 is the Faust-Henry constant [95], ω_{TO} = 409.7 and ω_{LO} = 574.2 cm^{-1} are the frequencies for quasi-TO (qTO) and quasi-LO (qLO) modes for ZnO NWs with a 6° vertical inclination [96,97]. For our LPP fitting model, the quasi-modes were used as an optimization due to the vertical inclination of 5.8 ± 4.5° seen on the cross-sectional view FESEM images of spontaneously grown ZnO NWs in **Fig. 1**, which is close to the average 6° inclination angle previously reported in Ref. [55]. The phonon damping constant (γ) of the A_1(LO) mode was assumed to be equal to the one of the non-polar E_2^{high} mode, deduced from the FWHM of the E_2^{high} Raman line. The free charge carrier density can then be determined by the plasmon frequency (ω_P) as follows:

$$\omega_P = \sqrt{\frac{4\pi e^2 \times n}{m^* \times \varepsilon_\infty}}$$

and the mobility is linked to the plasmon damping constant (γ_P) as follows:

$$\gamma_P = \frac{e}{m^*(E_F) \times \mu}$$

where m^* is the effective mass of electrons in the parabolic, isotropic conduction band and equals $0.23m_e$ at the Fermi level E_F [98]. As a result, the free charge carrier density and mobility are the only free parameters of the model.

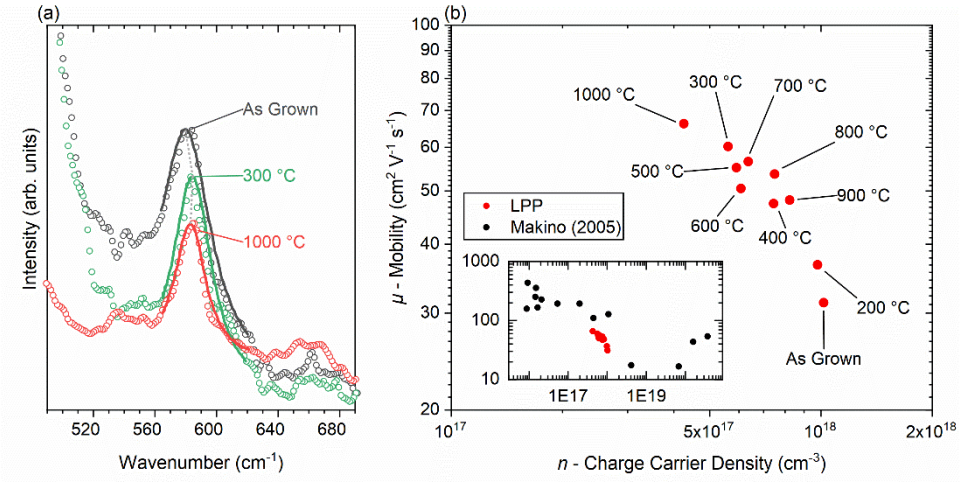

FIG. 9. (a) Theoretical calculation of the A_1(LO) phonon plasmon intensity using optimized parameters reported in Table 2 for as-grown (black solid line), 300 °C- (green solid line), and 1000 °C- (red solid line) annealed ZnO NWs for 1 h under oxygen atmosphere. The empty circles represent the corresponding acquired Raman spectra for as-grown (black), 300 °C- (green), and 1000 °C- (red) annealed ZnO NWs for 1 h under oxygen atmosphere. (b) Mobility vs free charge carrier density (red dots) in as-grown and annealed ZnO NWs from 200 to 1000 °C as deduced from the best LPP fit results. In the inset, Hall-effect measurements for un-doped and Ga-doped ZnO epitaxial thin films (black dots) are reported from Makino et al. [99] for comparison, along with the data of this work (red dots).

The LPP fits for the A_1(LO) mode in as-grown, 300 °C- and 1000 °C-annealed ZnO NWs are presented in **Fig. 9a**. The model was evaluated over a wide range of free charge carrier density and mobility from 1.0×10^{16} to 3.1×10^{19} cm^{-3} and 1 to 150 cm^2/V s, respectively, where the variation of the LPP fit from the A_1(LO) mode was calculated using a mean squared error method. The related two-dimensional error color maps, where pairs of free carrier density/mobility values give a reliable fit with a root mean squared error lower than 0.05, are shown in **Fig. S7**. The best LPP fits for the A_1(LO) mode in as-grown and annealed ZnO NWs are shown in **Fig. 9b**, along with the dedicated values for the fit parameters as summarized in **Table 2**.

Sample	A_1(LO) peak position (cm^{-1})	A_1(LO) FWHM (cm^{-1})	$\boldsymbol{\omega_P}$ (cm^{-1})	$\boldsymbol{\gamma}$ (cm^{-1})	$\boldsymbol{\gamma_P}$ (cm^{-1})	n ($\times 10^{17}$ cm^{-3})	μ (cm^2/V s)
As Grown	581.2	31.2	328.3	5.3	1295.0	10.2	31.3
200	582.2	37.4	322.0	4.9	1106.0	9.8	36.7
300	584.6	23.6	243.7	4.1	674.0	5.6	60.2
400	584.6	34.1	280.7	4.7	856.0	7.4	47.4
500	584.0	34.7	250.0	4.6	736.0	5.9	55.2
600	583.5	28.4	253.7	4.7	804.0	6.1	50.5
700	585.3	32.2	259.6	4.6	718.0	6.4	56.5
800	587.0	38.9	281.6	4.5	756.0	7.5	53.7
900	585.2	51.5	295.1	4.6	843.0	8.2	48.2

1000	583.3	27.2	212.3	4.2	613.0	4.3	66.2

TABLE 2. (a) LPP fit parameters in as-grown and annealed ZnO NWs for 1 h under oxygen atmosphere in the temperature range of 200 to 1000 °C.

The best LPP fit for as-grown ZnO NWs shows free charge carrier density and mobility values of $n = 1.02 \times 10^{18}$ cm^{-3} and $\mu = 31.3$ cm^2/V s, respectively, corresponding to a resistivity value of 195.7 mΩ cm. Using four-point probe resistivity measurements in the patterned metal configuration, a free charge carrier density ranging from 2.7×10^{18} to 3.1×10^{19} , and a resistivity ranging from 4.1 to 28.4 mΩ cm were reported in as-grown ZnO NWs grown by CBD under the spontaneous growth approach using the same conditions [14]. The apparent discrepancy between the resistivity values obtained from the best LPP fit and four-point probe measurements in as-grown ZnO NWs is explained in detail in **Fig. S8** and mainly originates from the oxygen species adsorbed on the NW surfaces during the Raman scattering measurement. It has been shown in Ref. [14] that the NWs show a metallic bulk-like electrical conduction dominated by the core. When probing an array of NWs by Raman scattering, an average LPP coupling is obtained due to the contributions from the core of the NW representing a flat-band regime, and the surface depleted region of the NW representing an upward band bending regime [88], where the free charge carrier density is considerably lower than in the bulk section due to the adsorbed oxygen species on the NW surfaces. Four-point probe resistivity measurements show a sudden increase in the resistivity of the NW due to its exposure to air. Resistivity values in as-grown ZnO NWs suddenly exposed to ambient conditions rise up from 70.3 to 100.3 mΩ cm, which fall in closer correlation with the 195.7 mΩ cm resistivity value obtained from the best LPP fit. The mobility values fall in the range of 31.3 to 66.2 cm^2/V s, which is in very good agreement with the typical values reported from FET measurements [100,101]. The smallest free charge carrier density of $n = 4.3 \times 10^{17}$ cm^{-3} together with the largest mobility of $\mu = 66.2$ cm^2/V s are obtained in ZnO NWs annealed at the highest temperature of 1000 °C, where the concentration of nitrogen- and hydrogen-related defects is by far the smallest one in the series of samples. It is worth noticing that the second smallest free carrier density of $n = 5.6 \times 10^{17}$ cm^{-3} and the second largest mobility of $\mu = 60.2$ cm^2/V s are obtained in ZnO NWs annealed at the

relatively low temperature of 300 °C, where the nitrogen-related defects exhibit one of the highest concentrations.

F. Effects of thermal annealing on nitrogen- and hydrogen-related defects

The effects of thermal annealing under oxygen atmosphere on the nature of nitrogen- and hydrogen-related defects in unintentionally-doped ZnO NWs by CBD are summarized in **Fig. 10**. The schematic illustration consists in an inclined top-view cross-section of one ZnO NW, where spheres represent single point defects and their association to form the nitrogen- and hydrogen-related defects distributed along the profile of the NW. It aims at representing the different mechanisms of reaction at work during thermal annealing at different temperatures from 200 to 1000 °C. The involvement of hydrogen, carbon, and nitrogen species along with their association gives rise to a large number of nitrogen- and hydrogen-related defects with different characteristics, as recapitulated in **Table 3**.

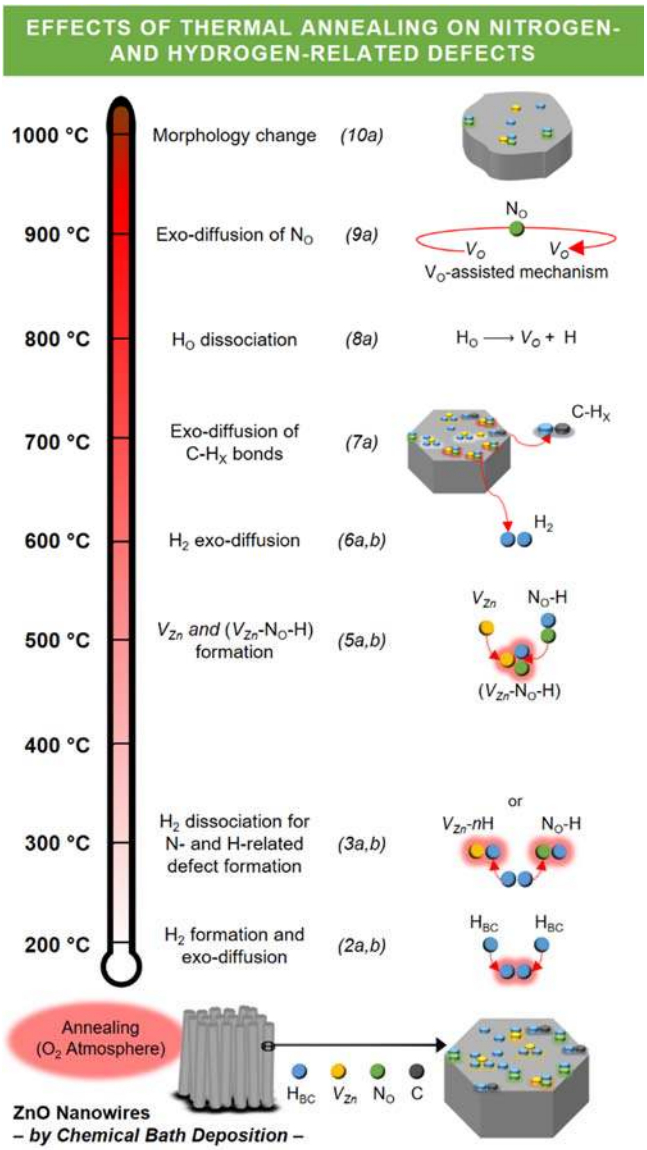

FIG. 10. Schematic illustration depicting the different mechanisms of reaction of nitrogen- and hydrogen-related defects at different annealing temperatures under oxygen atmosphere. (**2a,b**) shows the formation of H_2 molecules from two H_{BC} defects and the exo-diffusion of H_2 molecules at 200 °C. At 300 °C, H_2 molecules dissociate back into the H_{BC} defect (**3a**), and preferentially form other nitrogen- and hydrogen-related defects (**3b**). At 500 °C, V_{Zn} is formed (**5a**) and reacts with the N_O–H groups to create the (V_{Zn}-N_O-H) defect complex (**5b**). (**6a**) reveals the exo-diffusion of H_{BC} defects through the formation of H_2 molecules, while (**6b**) reports the further activation and generation of the (V_{Zn}-N_O-H) defect complex similarly to (**5b**). (**7a**) shows the exo-diffusion of C–H_X bonds at 700 °C. (**8a**) illustrates the dissociation of H_O and the related formation of V_O and H_{BC} at 800 °C. At 900 °C, N_O atoms exo-diffuse *via* a V_O-assisted mechanism through the formation of N_2 molecules (9a). At 1000 °C, a

morphology change is induced and the hexagonal shape is lost (**10a**). Note: the main nitrogen- and hydrogen-related defects are represented *via* the association of spheres representing single point defects for illustration purposes, hence no real scale is presented here.

The as-grown ZnO NWs show the presence of relevant and well-known hydrogen-related defects, including H_{BC}, (V_{Zn}-nH) defect complex with n=1-3, C–H_X, and N_O–H bonds [14], along with the (V_{Zn}-N_O-H) defect complex.

Following thermal annealing at the low temperature of 200 °C, a strong reduction of H_{BC} occurs, indicating the formation of electrically inactive H_2 molecules (**2a**) [34] which can either be trapped in the center of ZnO NWs or exo-diffuse if located nearby their surfaces (**2b**). The (N_O-H) defect complexes are also affected strongly and their concentration is significantly reduced as well as the (V_{Zn}-N_O-H) defect complex, but to a much smaller extent. Further thermal annealing at 300 °C results in the dissociation of H_2 molecules and makes energetically more favorable H_i (**3a**) [34], which can either rest as H_{BC} or be preferentially trapped by other nitrogen- and hydrogen-related defects to form the (V_{Zn}-nH) defect complexes with n= 1-3 and N_O–H groups (**3b**). It appears that the free charge carrier density in ZnO NWs is significantly reduced here and reaches the second smallest value. This is due to the redistribution of the nitrogen- and hydrogen-related defects, for which the nature differs and involves shallow donors and deep acceptors. These behaviors have clearly been shown and discussed in the framework of **Figs. 3** and **7**.

Following thermal annealing at 500 °C, the activation and generation of (V_{Zn}-N_O-H) defect complex with the -2 charge state is revealed through the formation of V_{Zn} at high temperatures (**5a**) and its reaction with the N_O–H groups (**5b**). The broadening of the NBE emission in the CL spectrum along with the sharp increase in the relative intensity of the green-blue emission band are strong evidences [69,76,102]. At the annealing temperature of 600 °C, an exo-diffusion phenomenon of H_{BC} in the form of H_2 molecules is expected to some extent (**6a**), together with the further activation and generation of the (V_{Zn}-N_O-H) defect complex (**6b**). The important contribution of the (V_{Zn}-N_O-H) defect complex through the predominance of ($A°X_A$) transitions in the NBE emission is strong evidence [69]. Further annealing in the range of 700 to 900 °C results in an interplay between the activation, and formation of (V_{Zn}-N_O-

H) defect complex, owing to the observed ($A^{\circ}X_A$) [82,83], DAP [84-86], and FA [87] transitions, as typically reported in nitrogen-doped ZnO films and NWs. Additionally, the vanishing of $C–H_X$ bonds trapped on the *m*-plane sidewalls of ZnO NWs is activated from the annealing temperature of 700 °C (**7a**).

The exo-diffusion phenomenon of N_O located in the bulk of ZnO at high annealing temperature has been proposed *via* an oxygen vacancy-assisted mechanism [77]. High temperature annealing under oxygen atmosphere is not favorable to the formation of oxygen vacancies, but the contribution of H_O should be taken into account here as its presence has already been noticed in ZnO nanorods grown by CBD with the same conditions [13]. Given that H_O is stable up to 800 °C [34], the high annealing temperatures could dissociate H_O and leads to its exo-diffusion, in turn leaving oxygen vacancies (**8a**) that could be involved in the suggested oxygen vacancy-assisted mechanism. The dissociation of nitrogen-related defects along with the oxygen vacancy-assisted mechanism (**9a**) and further binding of two interstitial nitrogen atoms would form a N_2 molecule [77], hence deactivating N_O. Finally, the thermal annealing at 1000 °C shows a clear morphology change where the hexagonal shape is lost (**10a**) and a strong decrease in the concentration of hydrogen-related defects is inferred, but the nitrogen-related defects still occur to some extent. The annihilation of the related visible emission bands is strong evidence. Interestingly, the clear NBE emission related to H_O *via* the I_4 line and its related TES shoulder at 1000 °C give an insight into its presence in ZnO NWs grown by CBD. Hence, correlating these findings**,** it can be stated that residual H_O, H_{BC}, V_{Zn}, (N_O–H) bonds, (V_{Zn}-N_O-H) defect complex are expected at 1000 °C, while the (V_{Zn}-*n*H) defect complexes with n=1-3 have completely vanished. It appears that the free charge carrier density is significantly decreased and reaches the smallest value of the series of samples.

	IR / Raman Modes (cm^{-1})	$E_{emission}$ (eV)			PL / CL (eV)
H_{BC}	330 / 3611 [a, b, c]	–	–		3.3601 [c]
H_O	273 [d]	–	–		3.3628 (I_4) [c]
V_{Zn}	–	ε(+2/+1) ε(+1/0) ε(0/-1)	2.53 [e] 2.48 [e] 2.19 [e]	2.40 [f] 1.90 [f] 1.29 [f]	1.60 [g, h]

		ε(-1/-2)	1.60 [e]	0.78 [f]	
(V_{Zn}-H)	3306 – 3418 [a, f]	ε(+2/+1) ε(+1/0) ε(0/-1)	2.49 [e] 2.40 [e] 1.82 [e]	2.35 [f] / 2.46 [i] 1.96 [f] / 1.81 [i] 1.31 [f] / 1.30 [i]	–
(V_{Zn}-2H)	3312 / 3349 [a]	ε(+2/+1) ε(+1/0)	2.46 [e] 2.29 [e]	2.30 [f] 2.08 [f] / 1.84 [i]	–
(V_{Zn}-3H)	3303 / 3321 [j]	ε(+1/0)	3.37 [e]		3.36143 (I_5) [k]
N_O–H ($AB_{N\perp}$)	3055 [l] / 3121 [m]	–	–		–
N_O–H ($AB_{N//}$)	3084 [l] / 3150 [n, o] / 3160 [m]	–	–		–
(V_{Zn}-N_O-H)	3078 [p, m]	ε(+1/0) ε(0/-1) ε(-1/-2)	2.50 [m] 2.27 [m] 1.82 [m]		–
C–H_X	2890, 2918, 2988 [q]	–	–		–
O–H	3500 [a, p]	–	–		–

TABLE 3. Recapitulating characteristics of the main nitrogen- and hydrogen-related defects with their respective Raman lines, $E_{emission}$ in luminescence spectroscopy using DFT calculations, and PL / CL lines. [a]Ref. [24], [b]Ref. [73], [c]Ref. [25], [d]Ref. [34], [e]Ref. [14] (GGA+*U* approach), [f]Ref. [53] (hybrid functionals), [g]Ref. [103], [h]Ref. [104], [i]Ref. [54] (hybrid functionals), [j]Ref. [75], [k]Ref. [27], [l]Ref. [39], [m]This Work (GGA + U approach), [n]Ref. [40], [o]Ref. [68], [p]Ref. [69], [q]Ref. [38].

IV. CONCLUSION

In summary, we have shown that the nitrogen- and hydrogen-related defects represent the major source of crystal defects in unintentionally-doped ZnO NWs grown by CBD owing to the large number of impurities contained in a growth medium. In addition to H_{BC}, H_O, and (V_{Zn}-*n*H) defect complexes, the nitrogen-related defects including (N_O-H) and (V_{Zn}-N_O-H) defect complexes also affect strongly the physical properties of ZnO NWs. In particular, the (V_{Zn}-N_O-H) defect complex acts as a deep acceptor with a relatively low formation energy and exhibits a prominent Raman line at 3078 cm^{-1} along with a red-orange emission energy of around 1.82 eV in cathodoluminescence spectroscopy. The N_O–H bonds in $AB_{N\perp}$ and $AB_{N||}$ configurations further lead to two Raman lines at 3121 and 3160 cm^{-1}, respectively. The tuning of the nitrogen- and hydrogen-related defects has been achieved using thermal annealing under oxygen atmosphere, resulting in a rather complex, fine evolution of their nature and concentration as a function of annealing temperature ranging from 200 to 1000 °C. Their resulting electrical properties

strongly depend on the balance between the nitrogen- and hydrogen-related defects and on their redistribution upon thermal annealing. ZnO NWs annealed at the moderate temperature of 300 °C specifically exhibit one of the smallest free charge carrier density of 5.6 x 10^{17} cm^{-3} along with a high mobility of about 60 cm^2/V s following the analysis of longitudinal optical phonon – plasmon coupling. A comprehensive diagram showing the complex interplay of each nitrogen- and hydrogen-related defect during thermal annealing and its dependence on the annealing temperature has been gained. Eventually, the engineering of the nitrogen- and hydrogen-related defects as the major source of crystal defects in unintentionally-doped ZnO NWs grown by CBD is capital to control their electronic structure properties governing their electrical and optical properties in any nanoscale engineering devices.

ACKNOWLEDGEMENTS

The authors would like to thank the financial support from the French National Research Agency through the project ROLLER (ANR-17-CE09-0033). J.V. held a doctoral fellowship from the ROLLER project. This research further benefited from some of the characterization equipment of the Grenoble INP-CMTC platform as well as from the CIMENT/GRICAD platform in Grenoble for computational resources. It was also supported by computational time granted from the Greek Research & Technology Network (GRNET) in the 'ARIS' National HPC infrastructure under the project AIMONACA (pr008002).

SUPPLEMENTAL MATERIAL

Raman spectra of unintentionally-doped ZnO NWs grown by CBD and annealed for 1 h under oxygen atmosphere in the temperature range of 200 to 1000 °C with a zoom-in in the area of interest at high wavenumber (FIG. S1); Evolution of the position and FWHM of the E_2^{high} Raman line of ZnO NWs as a function of the annealing temperature (FIG. S2); DOS of the (V_{Zn}-N_O-H) defect complex vs energy with a zoom-in in the area of interest (FIG. S3); Evolution of the position and FWHM of the NBE emission of ZnO NWs as a function of the annealing temperature (FIG. S4); Evolution of the acceptor-to-donor ratio (i.e. (V_{Zn}-N_O-H) to H_{BC}) deduced from the relative intensity ratio of each related Raman line of ZnO NWs as a function of the annealing temperature. (FIG. S5); Deconvolution of the visible emission bands in a typical cathodoluminescence spectrum of ZnO NWs using a Lorentzian function fit

(FIG. S6); Theoretical calculations of the A_1(LO) phonon plasmon intensity using optimized parameters for as-grown and annealed ZnO NWs for 1 h under oxygen atmosphere (FIG. S7);) *I–V* measurements using a four-point probe device on a single ZnO NW grown by CBD using the spontaneous growth approach under standard conditions. Four-point probe resistance to length ratio *R/l* as a function of the electron beam dose exposure of the single NW (FIG. S8).

[1] Z. L. Wang, Adv. Funct. Mater. **18**, 3553 (2008).
[2] V. Consonni and A. M. Lord, Nano Energy **83**, 105789 (2021).
[3] C. F. Pan, J. Y. Zhai, and Z. L. Wang, Chem. Rev. **119**, 9303 (2019).
[4] M. Willander *et al.*, Nanotechnology **20**, 40, 332001 (2009).
[5] V. Consonni, J. Briscoe, E. Karber, X. Li, and T. Cossuet, Nanotechnology **30**, 41, 362001 (2019).
[6] S. Rackauskas, N. Barbero, C. Barolo, and G. Viscardi, Nanomaterials **7**, 13, 381 (2017).
[7] L. Vayssieres, Adv. Mater. **15**, 464 (2003).
[8] K. M. McPeak, M. A. Becker, N. G. Britton, H. Majidi, B. A. Bunker, and J. B. Baxter, Chem. Mater. **22**, 6162 (2010).
[9] J. J. Cheng, S. M. Nicaise, K. K. Berggren, and S. Gradecak, Nano Lett. **16**, 753 (2016).
[10] C. Lausecker, B. Salem, X. Baillin, and V. Consonni, J. Phys. Chem. C **123**, 29476 (2019).
[11] X. H. Huang, Z. Y. Zhan, K. P. Pramoda, C. Zhang, L. X. Zheng, and S. J. Chua, Crystengcomm **14**, 5163 (2012).
[12] E. G. Barbagiovanni, R. Reitano, G. Franzo, V. Strano, A. Terrasi, and S. Mirabella, Nanoscale **8**, 995 (2016).
[13] T. Cossuet, F. Donatini, A. M. Lord, E. Appert, J. Pernot, and V. Consonni, J. Phys. Chem. C **122**, 22767 (2018).
[14] J. Villafuerte, F. Donatini, J. Kioseoglou, E. Sarigiannidou, O. Chaix-Pluchery, J. Pernot, and V. Consonni, J. Phys. Chem. C 124, 16652 (2020).
[15] J. B. Baxter and C. A. Schmuttenmaer, J. Phys. Chem. B **110**, 25229 (2006).
[16] A. M. Lord, T. G. Maffeis, A. S. Walton, D. M. Kepaptsoglou, Q. M. Ramasse, M. B. Ward, J. Koble, and S. P. Wilks, Nanotechnology **24**, 9, 435706 (2013).
[17] C. Opoku, A. S. Dahiya, F. Cayrel, G. Poulin-Vittrant, D. Alquier, and N. Camara, RSC Adv. **5**, 69925 (2015).
[18] L. Wang, S. Guillemin, J. M. Chauveau, V. Sallet, F. Jomard, R. Brenier, V. Consonni, and G. Bremond, Phys. Status Solidi 13, 576 (2016).
[19] C. G. Van de Walle, Phys. Rev. Lett. **85**, 1012 (2000).
[20] A. Janotti and C. G. Van de Walle, Nat. Mater. **6**, 44 (2007).
[21] M. G. Wardle, J. P. Goss, and P. R. Briddon, Phys. Rev. B **72**, 13, 155108 (2005).
[22] S. Z. Karazhanov, E. S. Marstein, and A. Holt, J. Appl. Phys. **105**, 4, 033712 (2009).
[23] D. M. Hofmann, A. Hofstaetter, F. Leiter, H. J. Zhou, F. Henecker, B. K. Meyer, S. B. Orlinskii, J. Schmidt, and P. G. Baranov, Phys. Rev. Lett. **88**, 4, 045504 (2002).
[24] E. V. Lavrov, J. Weber, F. Borrnert, C. G. Van de Walle, and R. Helbig, Phys. Rev. B **66**, 7, 165205 (2002).
[25] E. V. Lavrov, F. Herklotz, and J. Weber, Phys. Rev. B **79**, 13, 165210 (2009).
[26] B. K. Meyer *et al.*, Phys. Status Solidi B-Basic Solid State Phys. **241**, 231 (2004).
[27] R. Heinhold, A. Neiman, J. V. Kennedy, A. Markwitz, R. J. Reeves, and M. W. Allen, Phys. Rev. B **95**, 13, 054120 (2017).
[28] Y. Gao and Z. L. Wang, Nano Lett. **9**, 1103 (2009).

[29] G. Romano, G. Mantini, A. Di Carlo, A. D'Amico, C. Falconi, and Z. L. Wang, Nanotechnology **22**, 6, 465401 (2011).
[30] R. Hinchet, S. Lee, G. Ardila, L. Montes, M. Mouis, and Z. L. Wang, Adv. Funct. Mater. **24**, 971 (2014).
[31] G. Tian *et al.*, Nano Lett. **20**, 4270 (2020).
[32] J. I. Sohn *et al.*, Energy Environ. Sci. **6**, 97 (2013).
[33] R. Tao, M. Mouis, and G. Ardila, Adv. Electron. Mater. **4**, 9, 1700299 (2018).
[34] S. G. Koch, E. V. Lavrov, and J. Weber, Phys. Rev. B **89**, 8, 235203 (2014).
[35] X. H. Huang, C. B. Tay, Z. Y. Zhan, C. Zhang, L. X. Zheng, T. Venkatesan, and S. J. Chua, Crystengcomm **13**, 7032 (2011).
[36] Z. N. Urgessa *et al.*, J. Appl. Phys. **116**, 10, 123506 (2014).
[37] A. M. Lord, V. Consonni, T. Cossuet, F. Donatini, and S. P. Wilks, ACS Appl. Mater. Interfaces **12**, 13217 (2020).
[38] N. H. Nickel and K. Fleischer, Phys. Rev. Lett. **90**, 4, 197402 (2003).
[39] X. N. Li, B. Keyes, S. Asher, S. B. Zhang, S. H. Wei, T. J. Coutts, S. Limpijumnong, and C. G. Van de Walle, Appl. Phys. Lett. **86**, 3, 122107 (2005).
[40] S. J. Jokela and M. D. McCluskey, Phys. Rev. B **76**, 4, 193201 (2007).
[41] S. J. Jokela and M. D. McCluskey, J. Appl. Phys. **107**, 5, 113536 (2010).
[42] P. E. Blochl, Phys. Rev. B **50**, 17953 (1994).
[43] G. Kresse and D. Joubert, Phys. Rev. B **59**, 1758 (1999).
[44] J. P. Perdew, K. Burke, and M. Ernzerhof, Phys. Rev. Lett. **77**, 3865 (1996).
[45] J. P. Perdew, K. Burke, and M. Ernzerhof, Phys. Rev. Lett. **78**, 1396 (1997).
[46] K. Harun, N. A. Salleh, B. Deghfel, M. K. Yaakob, and A. A. Mohamad, Results in Physics **16**, 102829 (2020).
[47] N. N. Lathiotakis, A. N. Andriotis, and M. Menon, Phys. Rev. B **78**, 4, 193311 (2008).
[48] R. M. Sheetz, I. Ponomareva, E. Richter, A. N. Andriotis, and M. Menon, Phys. Rev. B **80**, 4, 195314 (2009).
[49] K. J. May and A. M. Kolpak, Phys. Rev. B **101**, 165117 (2020).
[50] I. S. Elfimov, A. Rusydi, S. I. Csiszar, Z. Hu, H. H. Hsieh, H. J. Lin, C. T. Chen, R. Liang, and G. A. Sawatzky, Phys. Rev. Lett. **98**, 137202 (2007).
[51] S. S. Parhizgar and J. Beheshtian, Computational Condens. Matter **15**, 1 (2018).
[52] A. Janotti and C. G. Van de Walle, Rep. Prog. Phys. **72**, 29, 126501 (2009).
[53] J. L. Lyons, J. B. Varley, D. Steiauf, A. Janotti, and C. G. Van de Walle, J. Appl. Phys. **122**, 12, 035704 (2017).
[54] Y. K. Frodason, K. M. Johansen, T. S. Bjorheim, B. G. Svensson, and A. Alkauskas, Phys. Rev. B **97**, 8, 104109 (2018).
[55] S. Guillemin, E. Appert, H. Roussel, B. Doisneau, R. Parize, T. Boudou, G. Bremond, and V. Consonni, J. Phys. Chem. C **119**, 21694 (2015).
[56] R. Parize, J. Garnier, O. Chaix-Pluchery, C. Verrier, E. Appert, and V. Consonni, J. Phys. Chem. C **120**, 5242 (2016).
[57] S. Guillemin, V. Consonni, E. Appert, E. Puyoo, L. Rapenne, and H. Roussel, J. Phys. Chem. C **116**, 25106 (2012).
[58] G. Guisbiers and S. Pereira, Nanotechnology **18**, 6, 435710 (2007).
[59] S. Guillemin, E. Sarigiannidou, E. Appert, F. Donatini, G. Renou, G. Bremond, and V. Consonni, Nanoscale **7**, 16994 (2015).
[60] R. Cusco, E. Alarcon-Llado, J. Ibanez, L. Artus, J. Jimenez, B. G. Wang, and M. J. Callahan, Phys. Rev. B **75**, 11, 165202 (2007).
[61] C. Bundesmann, N. Ashkenov, M. Schubert, D. Spemann, T. Butz, E. M. Kaidashev, M. Lorenz, and M. Grundmann, Appl. Phys. Lett. **83**, 1974 (2003).
[62] C. Verrier, E. Appert, O. Chaix-Pluchery, L. Rapenne, Q. Rafhay, A. Kaminski-Cachopo, and V. Consonni, Inorg. Chem. **56**, 13111 (2017).

[63] P. Gaffuri, E. Appert, O. Chaix-Pluchery, L. Rapenne, M. Salaun, and V. Consonni, Inorg. Chem. **58**, 10269 (2019).
[64] A. Kaschner *et al.*, Appl. Phys. Lett. **80**, 1909 (2002).
[65] A. Sugunan, H. C. Warad, M. Boman, and J. Dutta, J. Sol-Gel Sci. Techn. **39**, 49 (2006).
[66] V. Strano, R. G. Urso, M. Scuderi, K. O. Iwu, F. Simone, E. Ciliberto, C. Spinella, and S. Mirabella, J. Phys. Chem. C **118**, 28189 (2014).
[67] J. Hu, H. Y. He, and B. C. Pan, J. Appl. Phys. **103**, 4, 113706 (2008).
[68] O. S. Kumar, E. Watanabe, R. Nakai, N. Nishimoto, and Y. Fujita, J. Cryst. Growth **298**, 491 (2007).
[69] J. G. Reynolds, C. L. Reynolds, A. Mohanta, J. F. Muth, J. E. Rowe, H. O. Everitt, and D. E. Aspnes, Appl. Phys. Lett. **102**, 5, 152114 (2013).
[70] L. Liu *et al.*, Phys. Rev. Lett. **108**, 5, 215501 (2012).
[71] M. N. Amini, R. Saniz, D. Lamoen, and B. Partoens, Phys. Chem. Chem. Phys. **17**, 5485 (2015).
[72] D. Y. Yong, H. Y. He, Z. K. Tang, S. H. Wei, and B. C. Pan, Phys. Rev. B **92**, 5, 235207 (2015).
[73] E. V. Lavrov, F. Borrnert, and J. Weber, Phys. Rev. B **71**, 6, 035205 (2005).
[74] E. V. Lavrov, Physica B **340**, 195 (2003).
[75] F. Herklotz, A. Hupfer, K. M. Johansen, B. G. Svensson, S. G. Koch, and E. V. Lavrov, Phys. Rev. B **92**, 10, 155203 (2015).
[76] J. Y. Gao, X. Z. Zhang, Y. H. Sun, Q. Zhao, and D. P. Yu, Nanotechnology **21**, 8, 245703 (2010).
[77] J. Y. Gao, R. Qin, G. F. Luo, J. Lu, Y. Leprince-Wang, H. Q. Ye, Z. M. Liao, Q. Zhao, and D. P. Yu, Phys. Lett. A **374**, 3546 (2010).
[78] M. G. Wardle, J. P. Goss, and P. R. Briddon, Phys. Rev. Lett. **96**, 4, 205504 (2006).
[79] U. Herath, P. Tavadze, X. He, E. Bousquet, S. Singh, F. Muñoz, and A. H. Romero, Computer Physics Communications **251**, 107080 (2020).
[80] A. Teke, U. Ozgur, S. Dogan, X. Gu, H. Morkoc, B. Nemeth, J. Nause, and H. O. Everitt, Phys. Rev. B **70**, 10, 195207 (2004).
[81] Y. G. Wang, S. P. Lau, H. W. Lee, S. F. Yu, B. K. Tay, X. H. Zhang, and H. H. Hng, J. Appl. Phys. **94**, 354 (2003).
[82] D. C. Look, D. C. Reynolds, C. W. Litton, R. L. Jones, D. B. Eason, and G. Cantwell, Appl. Phys. Lett. **81**, 1830 (2002).
[83] X. D. Yang, Z. Y. Xu, Z. Sun, B. Q. Sun, L. Ding, F. Z. Wang, and Z. Z. Ye, J. Appl. Phys. **99**, 3, 046101 (2006).
[84] J. F. Rommeluere, L. Svob, F. Jomard, J. Mimila-Arroyo, A. Lusson, V. Sallet, and Y. Marfaing, Appl. Phys. Lett. **83**, 287 (2003).
[85] D. Pfisterer, J. Sann, D. M. Hofmann, M. Plana, A. Neumann, M. Lerch, and B. K. Meyer, Phys. Status Solidi B-Basic Solid State Phys. **243**, R1 (2006).
[86] B. P. Zhang, N. T. Binh, Y. Segawa, K. Wakatsuki, and N. Usami, Appl. Phys. Lett. **83**, 1635 (2003).
[87] J. W. Sun *et al.*, J. Appl. Phys. **102**, 6, 043522 (2007).
[88] C. Soci, A. Zhang, B. Xiang, S. A. Dayeh, D. P. R. Aplin, J. Park, X. Y. Bao, Y. H. Lo, and D. Wang, Nano Lett. **7**, 1003 (2007).
[89] H. Harima, S. Nakashima, and T. Uemura, J. Appl. Phys. **78**, 1996 (1995).
[90] T. Kozawa, T. Kachi, H. Kano, Y. Taga, M. Hashimoto, N. Koide, and K. Manabe, J. Appl. Phys. **75**, 1098 (1994).
[91] P. Perlin, J. Camassel, W. Knap, T. Taliercio, J. C. Chervin, T. Suski, I. Grzegory, and S. Porowski, Appl. Phys. Lett. **67**, 2524 (1995).
[92] P. Tchoulfian, F. Donatini, F. Levy, B. Amstatt, A. Dussaigne, P. Ferret, E. Bustarret, and J. Pernot, Appl. Phys. Lett. **103**, 5, 202101 (2013).
[93] A. J. Cheng *et al.*, J. Appl. Phys. **105**, 7, 073104 (2009).
[94] H. Yoshikawa and S. Adachi, Jpn. J. Appl. Phys. Part 1 - Regul. Pap. Brief Commun. Rev. Pap. **36**, 6237 (1997).
[95] B. H. Bairamov, A. Heinrich, G. Irmer, V. V. Toporov, and E. Ziegler, Phys. Status Solidi B-Basic Res. **119**, 227 (1983).

[96] R. Loudon, Adv. Phys. **50**, 813 (2001).
[97] T. Cossuet, H. Roussel, J. M. Chauveau, O. Chaix-Pluchery, J. L. Thomassin, E. Appert, and V. Consonni, Nanotechnology **29**, 11, 475601 (2018).
[98] M. Oshikiri, Y. Imanaka, F. Aryasetiawan, and G. Kido, Physica B **298**, 472 (2001).
[99] T. Makino, Y. Segawa, A. Tsukazaki, A. Ohtomo, and M. Kawasaki, Appl. Phys. Lett. **87**, 3, 022101 (2005).
[100] W. I. Park, J. S. Kim, G. C. Yi, M. H. Bae, and H. J. Lee, Appl. Phys. Lett. **85**, 5052 (2004).
[101] D. Kalblein, R. T. Weitz, H. J. Bottcher, F. Ante, U. Zschieschang, K. Kern, and H. Klauk, Nano Lett. **11**, 5309 (2011).
[102] R. Kobayashi, T. Kishi, Y. Katayanagi, T. Yano, and N. Matsushita, RSC Adv. **8**, 23599 (2018).
[103] X. J. Wang, L. S. Vlasenko, S. J. Pearton, W. M. Chen, and I. A. Buyanova, J. Phys. D: Appl. Phys. **42**, 175411 (2009).
[104] Y. Dong, F. Tuomisto, B. G. Svensson, A. Y. Kuznetsov, and L. J. Brillson, Phys. Rev. B **81**, 081201 (2010).